LAWRENCE
LIVERMORE
NATIONAL
LABORATORY

UCRL-JRNL-223449

A Core-Particle Model for Periodically Focused Ion Beams with Intense Space-Charge

S. M. Lund, J. J. Barnard, B. Bukh, S. R. Chawla, S. H. Chilton

August 7, 2006

Nuclear Instruments and Methods A

Disclaimer

A core-particle model for periodically focused ion beams with intense space-charge

Steven M. Lund, [a] John J. Barnard, [a] Boris Bukh [b]
Sugreev R. Chawla, [c] Sven H. Chilton [a,c]

[a] *Lawrence Livermore National Laboratory, Livermore, CA 94550, USA*
[b] *Princeton University, Princeton, NJ 08544, USA*
[c] *Lawrence Berkeley National Laboratory, Berkeley, CA 94720, USA*

Abstract

A core-particle model is derived to analyze transverse orbits of test particles evolving in the presence of a core ion beam described by the KV distribution. The core beam has uniform density within an elliptical cross-section and can be applied to model both quadrupole and solenoidal focused beams in periodic or aperiodic lattices. Efficient analytical descriptions of electrostatic space-charge fields external to the beam core are derived to simplify model equations. Image charge effects are analyzed for an elliptical beam centered in a round, conducting pipe to estimate model corrections resulting from image charge nonlinearities. Transformations are employed to remove coherent flutter motion associated with oscillations of the ion beam core due to rapidly varying, linear applied focusing forces. Diagnostics for particle trajectories, Poincaré phase-space projections, and single-particle emittances based on these transformations better illustrate the effects of nonlinear forces acting on particles evolving outside the core. A numerical code has been written based on this model. Example applications illustrate model characteristics. The core-particle model described has recently been applied to identify physical processes leading to space-charge transport limits for an rms matched beam in a periodic quadrupole focusing channel [Lund and Chawla, Nuc. Instr. and Meth. A **561**, 203 (2006)]. Further characteristics of these processes are presented here.

Key words: intense beam, space charge, emittance growth, simulation
PACS: 29.27.Bd, 41.75.-i, 52.59.Sa, 52.27.Jt

Email address: SMLund@llnl.gov (Steven M. Lund,).

1 Introduction

Core-particle (CP) models constitute a highly reduced description of beam evolution where single particles are analyzed that evolve both inside and outside a continuous core distribution with specified properties. Contributions of the test particles to the beam self-field are neglected, rendering the model inconsistent. CP models based on a core Kapchinskij-Vladimirskij (KV) distribution with uniform space-charge have had considerable success in predicting the maximum amplitude of halo particles evolving outside an envelope mismatched beam core with high space-charge intensity[1–4]. Recent work with a KV distribution based CP model applied to a matched envelope beam core[5] refines earlier related work[6,7] and suggests that long-observed space-charge related transport limits of a quadrupole focused beam result from strong resonance effects that allow significant populations of near-edge particles to undergo rapid chaotic transport to larger oscillation amplitudes due to overlapping resonances that approach the beam core. The main drawback of KV-based CP models is that they provide no consistent mechanism for particles launched within the core distribution to evolve outside the core. Effects outside the model must be appealed to for this purpose. Consequently, general predictions made with CP models should be carefully checked with fully self-consistent simulations. Nevertheless, the simplicity of the model facilitates analysis of characteristic particle orbits that can, in turn, aid interpretation of complicated transport limiting processes such as halo production, particle losses, and contributions to beam rms emittance growth from particles evolving outside the beam core.

Uniform density core beams modeled by the self-consistent KV distribution have typically been employed in CP models. This approach has advantages in that the evolution of the beam core can be simply described in terms of the evolution of the beam edge. Envelope equations that describe the edge evolution of the KV beam core are coupled ordinary differential equations that are well understood both in terms of the matched envelope (i.e., the beam edge has the periodicity of the focusing lattice) and any mismatch perturbations[8,9]. The KV distribution is presently the only known exact equilibrium solution to Vlasov's equation in a periodic focusing lattice. Alternative models for nonuniform beam cores have been proposed, often by assuming a self-similarly evolving nonuniform density profile core (see for example, Refs. [10,11] and references therein). Such distributions are not consistent core equilibria and are unlikely to approximate the physical Vlasov evolution of a realistic core where the collective wave response is generally expected to be such that the form of the density profile evolves from the initial state. Normal mode calculations with simple (continuous focusing model) equilibrium distributions suggest that perturbations will generally evolve with wavelengths incommensurate with the lattice period in a periodic transport channel[12,13]. Hence

it is highly improbable that an initial density nonuniformity can project on a spectrum of normal mode perturbations that add together to produce a self-similarly evolving beam density profile.

For a particle moving both inside and outside a core distribution, forces acting on core-particle model test particles will result from the linear applied focusing fields of the lattice and space-charge fields generated by the core. The applied field forces rapidly oscillate in a periodic focusing lattice. The space-charge forces produced by the core can be resolved as being a component due to a uniform density, rms-equivalent beam with elliptical envelope plus a component due to the difference between the actual and uniform beam distribution. For the uniform component, the fields exterior to the beam will be highly nonlinear and the fields interior to the beam will be linear. Both the interior and exterior components will oscillate with the variation of the elliptical envelope in response to applied focusing forces of the lattice and self-field defocusing forces. The impulse imparted by these oscillating linear forces of the core on a test particle traversing the core can increase or decrease the energy of the particle depending on the phase of the oscillation of the particle through the core. The self-fields generated by the nonuniform density component will rapidly oscillate (the collective response will be at harmonics of the plasma frequency) producing nonlinear fields both interior and exterior to the edge of the beam core. Collective mode decompositions of the nonuniform density perturbations will have normal mode components with a broad spectrum of wavelengths incommensurate with the lattice period. Since the nonuniform density component carries zero net charge, it is expected to only weakly perturb the external forces generated by the uniform density produced external forces except for when the particle is close to the edge of the core and nonuniformities are large. (By Gauss' Law the nonuniformities will produce zero perturbations external to the core of an axisymmetric beam.) The interior nonlinear forces produced by the nonuniform density component will oscillate rapidly within the lattice period and one would expect for limited amplitudes and distributed phases of the mode components that these perturbations will impart minimal net impulse on particles diving in and out of the core over several periods of the lattice. This random phase argument will also apply to external force components, further lessening the external influence of the nonuniformities. These effects lead one to believe that KV distribution based CP models should be reliable for strongly expressed resonances of a particle diving in and out of a realistic space-charge dominated core distribution where the density profile is expected to be relatively uniform due to Debye screening effects[12], phase mixing, Landau damping, and various nonlinear relaxation processes[14].

Here, we derive an efficient CP model to calculate trajectories of test "halo" particles evolving both inside and outside a uniform density elliptical beam with linear applied focusing forces varying arbitrarily in the axial coordinate

s. This model is applied to periodic focusing lattices to analyze strong chaotic processes that can allow particles moving just outside the beam edge to rapidly increase in oscillation amplitude. Recent studies have shown that such processes can be involved to explain space-charge transport limits that result from statistical beam emittance blow-up and particle losses[15,5].

The organization of this paper is the following. An efficient core-particle model for a test particle moving inside and outside a uniform density elliptical beam core is derived in Sec. 2. Effects of both s-varying applied fields and space-charge fields (direct and image) generated by the core are analyzed. Diagnostics and a numerical code implementation are discussed. Example applications of this model are presented in Sec. 3 to illustrate processes leading to space-charge transport limits associated with matched beams propagating in periodic quadrupole and solenoidal focusing lattices. Concluding comments in Sec. 4 summarize how the model can be applied to analyze space-charge related transport transport limits due to beam emittance growth and particle losses.

2 Core-Particle Model

We assume a continuous, unbunched ion beam core propagating in an arbitrary linear transport lattice. The axial coordinate is s and the linear applied focusing fields of the lattice are described by focusing functions $\kappa_j(s)$ with $j = x,\ y$. A test ion of charge q and mass m with axial relativistic factors $\beta_b = \text{const}$ and $\gamma_b = 1/\sqrt{1-\beta_b^2}$ moves in the presence of the core beam and the applied focusing forces. In the paraxial approximation, the transverse coordinates $x(s)$ and $y(s)$ of the test particle evolve according to the equations of motion[9,8]

$$\begin{aligned} x'' + \kappa_x x &= -\frac{q}{m\gamma_b^3\beta_b^2c^2}\frac{\partial\phi}{\partial x}, \\ y'' + \kappa_y y &= -\frac{q}{m\gamma_b^3\beta_b^2c^2}\frac{\partial\phi}{\partial y}. \end{aligned} \tag{1}$$

Here, primes denote derivatives with respect to s, c is the speed of light *in vacuo*, and ϕ is the electrostatic potential of the beam core. The potential is given in terms of the core charge density ρ by the solution to the transverse Poisson equation

$$\left(\frac{\partial^2}{\partial x^2} + \frac{\partial^2}{\partial y^2}\right)\phi = -\frac{\rho}{\epsilon_0}. \tag{2}$$

Here, ϵ_0 is the permitivity of free-space. Solutions for ϕ must satisfy boundary conditions ($\phi = \text{const}$) on any conducting surfaces associated with material apertures.

This formulation can be applied to a wide variety of focusing lattices including continuous ($\kappa_j = k_{\beta 0}^2 = \text{const}$), solenoidal ($\kappa_x = \kappa_y$), and quadrupole ($\kappa_x = -\kappa_y$) focusing. Specific forms for the focusing coefficient κ_j can be found in Ref. [9]. For solenoidal focusing, the particle orbits must be interpreted as being expressed in a rotating Larmor frame (see Appendix A of Ref. [9]). The lattice need not be periodic. For periodic lattices, the scales of the κ_j can always be set by the undepressed particle phase advances σ_{0j} (measured in degrees per lattice period). In lattices with sufficient plane-symmetry, $\sigma_{0x} = \sigma_{0y} \equiv \sigma_0$. Example piecewise constant FODO quadrupole and solenoidal focusing lattices that will be employed in examples in Sec. 3 are shown in Fig. 1. We denote the lattice period by L_p, the fractional occupancy of focusing elements in the period by $\eta \in (0, 1]$, and the drift distances between focusing elements by d. Formulas for setting σ_0 in simple lattices with piecewise constant κ_j can be found in the references.

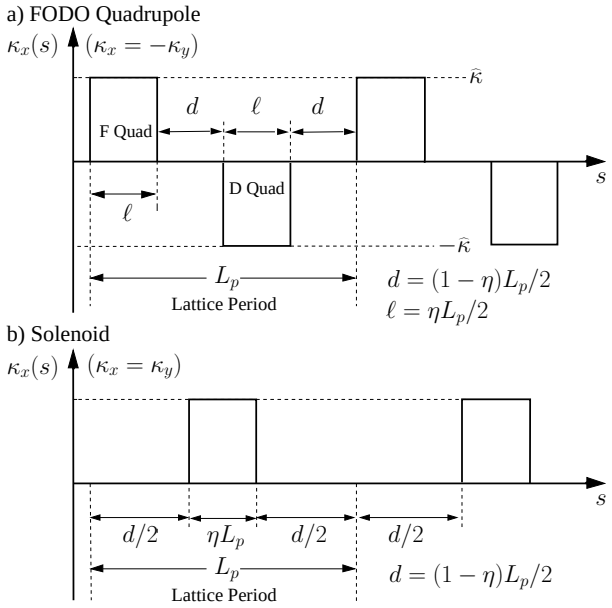

Fig. 1. Periodic focusing lattices for a) FODO quadrupole focusing, and b) solenoidal focusing.

Regardless of the structure of the charge density $\rho(\mathbf{x}_\perp)$ as a function of the transverse coordinate $\mathbf{x}_\perp = x\hat{\mathbf{x}} + y\hat{\mathbf{y}}$, the linearity of the Poisson equation (2) can be exploited to resolve the electric self-field of the beam as

$$\mathbf{E}_\perp = -\frac{\partial \phi}{\partial \mathbf{x}_\perp} = \mathbf{E}_\perp^d + \mathbf{E}_\perp^i, \tag{3}$$

where

$$\mathbf{E}_\perp^d(\mathbf{x}_\perp) = \frac{1}{2\pi\epsilon_0} \int d^2\tilde{x}_\perp \, \frac{\rho(\tilde{\mathbf{x}}_\perp)(\mathbf{x}_\perp - \tilde{\mathbf{x}}_\perp)}{|\mathbf{x}_\perp - \tilde{\mathbf{x}}_\perp|^2} \tag{4}$$

is the direct field produced by the beam charge density in free-space, and

$$\mathbf{E}_\perp^i(\mathbf{x}_\perp) = \frac{1}{2\pi\epsilon_0}\int d^2\tilde{x}_\perp \, \frac{\rho^i(\tilde{\mathbf{x}}_\perp)(\mathbf{x}_\perp - \tilde{\mathbf{x}}_\perp)}{|\mathbf{x}_\perp - \tilde{\mathbf{x}}_\perp|^2} \tag{5}$$

is the so-called image charge field produced by the induced charge density $\rho^i(\mathbf{x}_\perp)$ on the conducting aperture of the machine. The image charge field $\mathbf{E}_\perp^i$ depends both on the geometry of the machine aperture and on the distribution of beam space-charge internal to the aperture.

In a linear focusing system it is reasonable to expect an idealized beam to have elliptical symmetry charge density ρ, i.e., with ρ constant on surfaces with $(x/r_x)^2 + (y/r_y)^2 = \text{const}$. Here, the r_j are taken to be positive and the ratio r_x/r_y defines the ellipticity of ρ. Generally, the r_j will vary as a function of s consistent with the evolution of the core distribution. For such elliptical symmetry ρ, the direct field $\mathbf{E}_\perp^d$ produced by the beam core can be calculated in terms of a potential ϕ^d as $\mathbf{E}_\perp^d = \partial\phi^d/\partial\mathbf{x}_\perp$ with[16]

$$\phi^d = -\frac{r_x r_y}{4\epsilon_0}\int_0^\infty d\xi \, \frac{\Gamma(\chi)}{\sqrt{r_x^2+\xi}\sqrt{r_y^2+\xi}} + \text{const.} \tag{6}$$

Here, $\chi \equiv x^2/(r_x^2+\xi) + y^2/(r_y^2+\xi)$ and $\Gamma(\chi)$ is a function defined such that

$$\rho = \left.\frac{d\Gamma(\chi)}{d\chi}\right|_{\xi=0}. \tag{7}$$

An appropriate choice of Γ can always be made for elliptical symmetry ρ. It is straightforward to verify that Eqs. (6) and (7) satisfy the direct field Poisson equation $\frac{\partial^2\phi}{\partial\mathbf{x}_\perp^2} = -\frac{\rho}{\epsilon_0}$ for ρ with elliptical symmetry.

Motivated by the overview discussion in Sec. 1, we consider a uniform density beam core centered at $x = 0 = y$ with

$$\rho = \begin{cases} \frac{\lambda}{\pi r_x r_y}, & \frac{x^2}{r_x^2} + \frac{y^2}{r_y^2} \le 1, \\ 0, & \frac{x^2}{r_x^2} + \frac{y^2}{r_y^2} > 1. \end{cases} \tag{8}$$

Here, $\lambda = \text{const}$ is the beam line-charge density, and r_j are the edge radii of a uniform density elliptical beam. It is straightforward to verify that

$$\Gamma(\chi) = \frac{\lambda}{\pi r_x r_y}\begin{cases} \chi, & \chi \le 1, \\ 1, & \chi > 1, \end{cases} \tag{9}$$

produces the required uniform density elliptical core consistent with Eqs. (7)

and (8). Inserting Eq. (9) in (6) gives[17,12]

$$\phi^d = -\frac{\lambda}{4\pi\epsilon_0}\left\{\int_0^{\xi_b}\frac{d\xi}{\sqrt{r_x^2+\xi}\sqrt{r_y^2+\xi}}+ \int_{\xi_b}^{\infty}\frac{d\xi}{\sqrt{r_x^2+\xi}\sqrt{r_y^2+\xi}}\left(\frac{x^2}{r_x^2+\xi}+\frac{y^2}{r_y^2+\xi}\right)\right\}+\text{const}, \tag{10}$$

where $\xi_b = 0$ when $(x/r_x)^2+(y/r_y)^2 \le 1$ (within the core) and ξ_b is the positive root of

$$\frac{x^2}{r_x^2+\xi_b}+\frac{y^2}{r_y^2+\xi_b} = 1 \tag{11}$$

when $(x/r_x)^2 + (y/r_y)^2 > 1$ (outside the core). This gives *both* inside and outside the core,

$$\begin{aligned} E_x^d = -\frac{\partial\phi^d}{\partial x} =& \frac{\lambda}{2\pi\epsilon_0}\int_{\xi_b}^{\infty}\frac{d\xi}{\sqrt{r_x^2+\xi}\sqrt{r_y^2+\xi}}\frac{x}{r_x^2+\xi} \\ =& \frac{\lambda}{\pi\epsilon_0}\frac{x}{(r_x+r_y)r_x}F_x^d, \\ E_y^d = -\frac{\partial\phi^d}{\partial y} =& \frac{\lambda}{2\pi\epsilon_0}\int_{\xi_b}^{\infty}\frac{d\xi}{\sqrt{r_x^2+\xi}\sqrt{r_y^2+\xi}}\frac{y}{r_y^2+\xi} \\ =& \frac{\lambda}{\pi\epsilon_0}\frac{y}{(r_x+r_y)r_y}F_y^d, \end{aligned} \tag{12}$$

where F_j^d are direct field form factors given by

$$\begin{aligned} F_x^d =& \frac{r_x}{r_x-r_y}\left(1-\sqrt{\frac{r_y^2+\xi_b}{r_x^2+\xi_b}}\right), \\ F_y^d =& \frac{r_y}{r_y-r_x}\left(1-\sqrt{\frac{r_x^2+\xi_b}{r_y^2+\xi_b}}\right), \end{aligned} \tag{13}$$

and

$$\xi_b = \begin{cases} 0, & \frac{x^2}{r_x^2}+\frac{y^2}{r_y^2}\le 1, \\ -\frac{(r_x^2+r_y^2-x^2-y^2)}{2}+\frac{\sqrt{(r_x^2+r_y^2-x^2-y^2)^2-4(r_x^2r_y^2-x^2r_y^2-y^2r_x^2)}}{2}, & \frac{x^2}{r_x^2}+\frac{y^2}{r_y^2}>1. \end{cases} \tag{14}$$

Equations (12)–(14) for the direct fields have been employed in Eq. (1) with zero image fields by Wang[3] to analyze test particles evolving in the presence of a uniform density elliptical beam.

Interior to the beam core, $\xi_b = 0$ giving $F_j^d = 1$ and Eq. (12) reduces to the well-known result for the direct fields within a uniform density elliptical beam

with[18,12]

$$E_x^d = \frac{\lambda}{\pi\epsilon_0}\frac{x}{(r_x+r_y)r_x}, \qquad E_y^d = \frac{\lambda}{\pi\epsilon_0}\frac{y}{(r_x+r_y)r_y}. \tag{15}$$

Note that inside the beam E_x^d and E_y^d are linear functions of x and y. Exterior to the beam, $\xi_b \neq 0$ and the direct fields are complicated nonlinear functions of the coordinates and beam edge radii r_j. For the special case of a round beam ($r_x = r_y = r_b$), a limit analysis of Eqs. (12)–(14) for the exterior fields shows that

$$E_x^d = E_y^d = \frac{\lambda}{2\pi\epsilon_0 r} \tag{16}$$

with $r = \sqrt{x^2+y^2}$. The characteristic $1/r$ exterior ($r > r_b$) nonlinearity is consistent with the form expected from a direct application of Gauss' Law.

For a test particle evolving both inside and outside of the uniform density elliptical beam core, the equations of motion (1) can be conveniently expressed as

$$\begin{aligned} x'' + \kappa_x x &= \frac{2QF_x}{(r_x+r_y)r_x}x, \\ y'' + \kappa_y y &= \frac{2QF_y}{(r_x+r_y)r_y}y. \end{aligned} \tag{17}$$

Here,

$$F_j = F_j^d + F_j^i, \tag{18}$$

are form-factors due to due to direct (d) and image (i) contributions, and

$$Q = \frac{q\lambda}{2\pi\epsilon_0 m\gamma_b^3\beta_b^2 c^2} = \text{const} \tag{19}$$

is the dimensionless perveance[8]. Because $F_j = 1$ within a uniform density core beam without image charge effects, the form of Eq. (17) emphasizes nonlinear effects (i.e., $F_j \neq 1$ with variation in x and y) due to direct external fields and image charges.

An alternative calculation of the direct field $\mathbf{E}_\perp^d$ exterior to a uniform density elliptical beam can be carried out as follows to obtain a simpler expression than given by Eqs. (12)–(14). First, without loss in generality, Eq. (4) for the direct field can be expressed in complex form as

$$\underline{E}^d \equiv E_y^d + iE_x^d = \frac{i}{2\pi\epsilon_0}\int d^2\tilde{x}_\perp \, \frac{\rho(\tilde{\mathbf{x}}_\perp)}{\underline{z}-\underline{\tilde{z}}}. \tag{20}$$

Here, underlines denote complex quantities, $i \equiv \sqrt{-1}$, and $\underline{z} = x + iy$. Using an exterior multipole form expansion exterior to the beam obtains

$$\underline{E}^d = \sum_{n=1}^{\infty} \underline{C}_n \underline{z}^{-n} \tag{21}$$

with

$$\underline{C}_n = \frac{i}{2\pi\epsilon_0}\int d^2x_\perp\ \rho(\mathbf{x}_\perp)\underline{z}^{n-1}. \tag{22}$$

Exterior to beam, the direct field $\mathbf{E}_\perp^d$ satisfies the vacuum Maxwell equations $\nabla_\perp\cdot\mathbf{E}_\perp^d = 0$ and $\nabla_\perp\times\mathbf{E}_\perp^d = 0$. Or equivalently, the transverse field components satisfy

$$\frac{\partial E_x}{\partial x} = -\frac{\partial E_y}{\partial y}, \qquad \frac{\partial E_y}{\partial x} = \frac{\partial E_x}{\partial y}, \tag{23}$$

which can be recognized as the Cauchy-Riemann conditions for the complex field $\underline{E}^d = E_y^d + iE_x^d$ to be an analytical function of $\underline{z} = x+iy$. This analyticity of $\underline{E}^d(\underline{z})$ allows the series expansion given by Eqs. (21) and (22) to be applied in the *entire* vacuum region exterior to the elliptical beam core. Using the uniform density ρ defined by Eq. (8) in Eq. (22) obtains for $(x/r_x)^2 + (y/r_y)^2 > 1$

$$\underline{E}^d = \frac{i\lambda}{\pi\epsilon_0}\sum_{n=1,3,5,\cdots}^{\infty}\frac{(n-1)!}{2^n\left(\frac{n-1}{2}+1\right)!\left(\frac{n-1}{2}\right)!}\frac{(r_x^2-r_y^2)^{(n-1)/2}}{\underline{z}^n}. \tag{24}$$

This series can be summed and the form factor definitions applied to show that exterior to the beam

$$\begin{aligned} F_x^d &= (r_x+r_y)\frac{r_x}{x}\mathrm{Re}[\underline{S}], \\ F_y^d &= -(r_x+r_y)\frac{r_y}{y}\mathrm{Im}[\underline{S}], \end{aligned} \tag{25}$$

where

$$\begin{aligned} \underline{S} &\equiv \frac{\underline{z}}{r_x^2-r_y^2}\left[1-\sqrt{1-\frac{r_x^2-r_y^2}{\underline{z}^2}}\right] \\ &= \frac{1}{2\underline{z}}\left[1+\frac{1}{2}\frac{r_x^2-r_y^2}{\underline{z}^2}+\frac{1}{8}\frac{(r_x^2-r_y^2)^2}{\underline{z}^4}+\cdots\right]. \end{aligned} \tag{26}$$

The second expanded form of $\underline{S}$ in Eq. (26) is useful when then beam envelope is nearly round with $r_x \simeq r_y$. Note that for a round beam with $r_x = r_y = r_b$, only one term in the sum remains giving $\underline{S} = (x-iy)/(2r^2)$ with $F_j^d = r_b^2/r^2$. After some manipulation, it can be shown that the form factors given by Eqs. (13) and (25) are identical. The complex form expression (25) can be more efficient to employ in numerical studies.

Unfortunately, explicit evaluation of the image field described by Eq. (5) is complicated and depends on aperture geometry. To estimate characteristic image field effects, we consider the simple case of a circular aperture of radius r_p centered at $\mathbf{x}_\perp = 0$. Then the image induced by the charge density $\rho(\mathbf{x}_\perp)$ is $\rho^i = -\rho$ at location $\mathbf{x}_\perp^i = r_p^2\mathbf{x}_\perp/|\mathbf{x}_\perp|^2$, and Eq. (5) gives

$$\mathbf{E}_\perp^i(\mathbf{x}_\perp) = -\frac{1}{2\pi\epsilon_0}\int_{\mathrm{pipe}} d^2\tilde{x}_\perp\ \frac{\rho(\tilde{\mathbf{x}}_\perp)(\mathbf{x}_\perp - r_p^2\tilde{\mathbf{x}}_\perp/|\tilde{\mathbf{x}}_\perp|^2)}{|\mathbf{x}_\perp - r_p^2\tilde{\mathbf{x}}_\perp/|\tilde{\mathbf{x}}_\perp|^2|^2}. \tag{27}$$

Two limiting forms of Eq. (27) can be examined to illustrate properties of the image field. First, to leading order, an off-axis beam can be approximated as being a line-charge displaced along the x-axis at $x = X$ with $|X| < r_p$ [i.e., $\rho(\mathbf{x}_\perp) = \lambda\delta(\mathbf{x}_\perp - X\hat{\mathbf{e}}_x)$]. Then the image field is

$$\mathbf{E}_\perp^i = -\frac{\lambda}{2\pi\epsilon_0}\frac{\mathbf{x}_\perp - r_p^2\frac{X}{X^2}\hat{\mathbf{e}}_x}{\left|\mathbf{x}_\perp - r_p^2\frac{X}{X^2}\hat{\mathbf{e}}_x\right|^2}. \tag{28}$$

For $r_p^2/|X|$ large, the image field $\mathbf{E}_\perp^i$ will generally be small relative to the direct field $\mathbf{E}_\perp^d \simeq \frac{\lambda}{2\pi\epsilon_0}\frac{\mathbf{x}_\perp}{|\mathbf{x}_\perp|^2}$. Next, we take ρ to be given by Eq. (8), corresponding to an uniform density, on-axis elliptical beam. In this limit, the image charge field of the uniform density beam can be explicitly calculated from Eq. (27) using complex variables (for notational convenience). Series expansion shows that within the aperture

$$\underline{E^i} = E_y^i + iE_x^i = \sum_{n=2,4,\cdots}^{\infty} \underline{C}_n \underline{z}^{n-1}, \tag{29}$$

where

$$\begin{aligned}\underline{C}_n &= \frac{i}{2\pi\epsilon_0}\int_{\text{pipe}} d^2x_\perp\ \rho(\mathbf{x}_\perp)\frac{(x-iy)^n}{r_p^{2n}} \\ &= \frac{i\lambda n!}{2\pi\epsilon_0 2^n(n/2+1)!(n/2)!}\left(\frac{r_x^2 - r_y^2}{r_p^4}\right)^{n/2}.\end{aligned} \tag{30}$$

The leading order $n = 2$ components of this image field are linear with

$$E_x^i = \frac{\lambda}{8\pi\epsilon_0}\frac{r_x^2 - r_y^2}{r_p^4}x, \qquad E_y^i = -\frac{\lambda}{8\pi\epsilon_0}\frac{r_x^2 - r_y^2}{r_p^4}y. \tag{31}$$

These expressions show that leading order linear image charge corrections produced for an on-axis elliptical beam are weak relative to the direct fields for small beam ellipticities with $|r_x/r_y - 1| \ll 1$ and/or a large pipe radius r_p. Motivated by these limiting case results, for present purposes of analyzing leading order effects, we take $F^i = 0$ and neglect image charge corrections. Results in the literature[19,11] can also be applied to calculate more elaborate image charge corrections.

To complete the core-particle model, evolution equations must be derived for the envelope radii r_j of the uniform density beam core. For the centered, on-axis beam with image charge effects neglected, the core can be self-consistently described by the KV distribution function where the envelope radii evolve according the KV envelope equations[9,8]

$$r_j'' + \kappa_j r_j - \frac{2Q}{r_x + r_y} - \frac{\varepsilon_j^2}{r_j^3} = 0. \tag{32}$$

Here,

$$\begin{aligned}\varepsilon_x &= 4\left[\langle x^2\rangle_\perp\langle x'^2\rangle_\perp - \langle xx'\rangle_\perp^2\right]^{1/2} = \text{const},\\ \varepsilon_y &= 4\left[\langle y^2\rangle_\perp\langle y'^2\rangle_\perp - \langle yy'\rangle_\perp^2\right]^{1/2} = \text{const},\end{aligned} \tag{33}$$

are the x- and y-plane rms edge emittances of a centered elliptical beam ($\langle x\rangle_\perp = 0 = \langle y\rangle_{!\perp}$) and $\langle\cdots\rangle_\perp$ denotes a transverse statistical average over the core distribution. For the case of a periodic lattice with lattice period L_p, $\kappa_j(s+L_p) = \kappa_j(s)$ and the beam core is said to be matched when the envelope radii r_j have the periodicity of the lattice

$$r_j(s + L_p) = r_j(s). \tag{34}$$

Envelope matching requires that the r_j satisfy appropriate initial conditions in the lattice. For a matched beam, the phase advance of particles moving with the KV beam core in the presence of linear applied focusing and space-charge defocusing forces can be calculated as[9]

$$\sigma_j = \varepsilon_j \int_{s_i}^{s_i+L_p} \frac{ds}{r_j^2(s)}, \tag{35}$$

independent of the initial value of $s = s_i$. The ratio of depressed to undepressed particle phase advance $\sigma_j/\sigma_{0j} \in (0, 1)$ provides a convenient, normalized measure of relative space-charge strength with $\sigma_j/\sigma_{0j} \to 1$ corresponding to negligible space-charge ($Q \to 0$ with ε_j finite), and $\sigma_j/\sigma_{0j} \to 0$ corresponding to maximum ($\varepsilon_j \to 0$ with Q finite) space-charge intensity. For systems with sufficient plane symmetry ($\sigma_{0j} = \sigma_0$ and $\varepsilon_x = \varepsilon_y$), we denote $\sigma_j/\sigma_{0j} = \sigma/\sigma_0$.

A *Mathematica*[20] based CP code was written to numerically integrate the particle equations of motion (17) from initial conditions using a symplectic ordinary differential equation solver. Tests verify that particles launched with initial conditions that are contained within maximum phase-space extent of the KV equilibrium core remain confined within the core as the particles evolve. The code numerically calculates the scale of the κ_j needed to achieve specified input values of σ_0 for a variety of periodic lattices (continuous, solenoid, FODO quadrupole, and quadrupole doublet, ...) with piecewise constant $\kappa_j(s)$ that are described in Ref. [9]. Beam cores with both matched and mismatched envelopes can be launched in periodic lattices. Matched envelopes are calculated using the methods described in Ref. [21] and are specified by the lattice type and lattice parameters (L_p, η, and σ_{0j}), and the depressed phase advances σ_j and emittances ε_j of the beam core. This parameterization allows convenient expression of the relative applied focusing and space-charge strength. Specific envelope mismatch modes can also be launched using formulations described in Ref. [9].

The CP code has extensive options to launch test particles at an arbitrary axial location s_i in the focusing lattice. Spatial coordinates of particles $\mathbf{x}_\perp(s_i)$

can be initialized along principal axes of the elliptical beam or within an annular region of specified extent in the radial and azimuthal coordinates $\xi = \sqrt{x^2/r_x^2 + y^2/r_y^2}$ and $\theta = \tan^{-1}(y, x)$. The initial coordinates can be randomly dispersed within the annular region or regularly distributed. We typically launch particles with initial x and y coordinates outside the beam edge (i.e., $x^2/r_x^2 + y^2/r_y^2 > 1$). Angles of particles $\mathbf{x}'_\perp(s_i)$ can be initialized with additive coherent and incoherent components. The coherent component is set consistently by extrapolating flows associated with the flutter of the KV equivalent core with

$$x' = r'_x \frac{x}{r_x}, \quad y' = r'_y \frac{y}{r_y}. \tag{36}$$

Incoherent angle contributions are randomly set by either uniform or Gaussian distributions with amplitudes set consistent with local rms spread values (i.e., "temperatures") that can vary with spatial coordinate in a specified manner.

Various diagnostics are implemented in the core-test particle code including: particle trajectories, single particle emittances defined by (for the x-plane, the y-plane is analogous)

$$\epsilon_x = \sqrt{\left(\frac{x}{r_x}\right)^2 + \left(\frac{r'_x x - x' r_x}{\varepsilon_x}\right)^2}, \tag{37}$$

stroboscopic Poincaré phase-space plots in various phase-space coordinates, and particle oscillation wavelengths calculated from Fourier transforms of orbits. The single particle emittance ϵ_x should not be confused with the statistical beam emittance ε_x. ϵ_x is normalized such that a particle oscillating in the x-plane has $\epsilon_x = 1$ when the particle touches the edge of the core distribution in x-x' phase-space. Particle trajectories and Poincaré phase-spaces can be plotted in scaled coordinates [e.g., with x–x' projections scaled as x/r_x–$(x'r_x - r'_x x)/\varepsilon_x$] to better illustrate oscillation extents relative to the matched beam core. To help determine if certain classes of initial conditions become excited to larger amplitude, diagnostics can be carried out for groups of test particles launched within specified ranges of the radial coordinate $\xi = \sqrt{x^2/r_x^2 + y^2/r_y^2}$.

Particles evolving both inside and outside the beam envelope will experience a substantial, space-charge dependent nonlinearity when moving exterior to the beam. To better illustrate this effect, the scaled radial force acting on particles for a continuously focused matched beam ($\kappa_j = (\sigma_0/L_p)^2$, $\varepsilon_x = \varepsilon_y$) of radius $r = r_b = \text{const}$ is plotted as a function of r/r_b. The force is proportional to $(\sigma_0^2/L_p^2)r - (QF_x^d/r_b^2)r$ and is produced by the applied focusing and space-charge defocusing forces. Note that the nonlinear force transition at $r/r_b = 1$ becomes stronger as relative space-charge strength increases (i.e., σ/σ_0 decreases) and there is no nonlinear transition for zero space-charge strength ($\sigma/\sigma_0 = 1$).

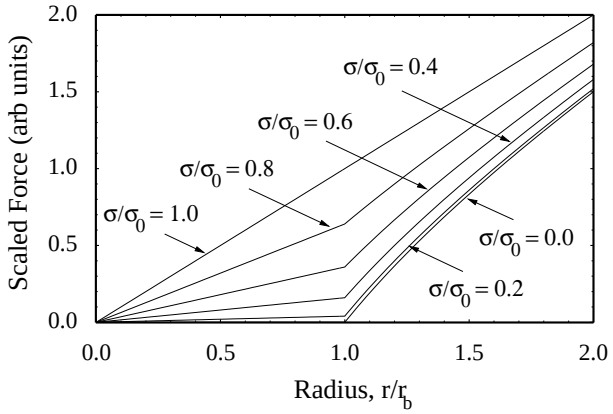

Fig. 2. Scaled radial force from applied and self-fields versus radial coordinate r for a round, uniform density continuously focused beam of radius $r = r_b$. Curves correspond to relative space-charge strengths $\sigma/\sigma_0 = 0$, 0.1, 0.2, $\cdots$, 1.0.

Nonlinear space-charge effects will be further enhanced by the periodic variations (flutter) of the envelope radii for a matched, elliptical beam in a periodic focusing lattice. For simple lattices with a high degree of symmetry, a measure of the flutter is given by $\mathrm{Max}[r_x]/\overline{r_x}$. Here, $\mathrm{Max}[r_x]$ is the maximum radial excursion of the matched envelope over the lattice period and $\overline{r_x} = (1/L_p)\int_0^{L_p} ds\; r_x$ is the average excursion of the matched envelope in the lattice period. Unfortunately, direct calculation of the envelope flutter is difficult since the envelope equation (32) is nonlinear. For a given lattice and a beam with $\varepsilon_j = \varepsilon$, the structure of the matched beam envelope will depend on the symmetry and strength of the focusing functions κ_j (with scale set by σ_0) and (more weakly) on ε and σ/σ_0[9]. Using the methods presented by Lee [22], it can be shown that the flutter of the matched beam envelope for periodic solenoidal and FODO quadrupole focusing systems with piecewise constant $\kappa_j(s)$ is given approximately for $\sigma/\sigma_0 \ll 1$ by

$$\frac{\mathrm{Max}[r_x]}{\overline{r_x}} - 1 \simeq \begin{cases} \frac{(1-\cos\sigma_0)^{1/2}(1-\eta/2)}{2^{3/2}(1-2\eta/3)^{1/2}} & \text{Quadrupole Focusing,} \\ \frac{(1-\cos\sigma_0)(1-\eta)(1-\eta/2)}{6} & \text{Solenoidal Focusing.} \end{cases} \tag{38}$$

Here, $\eta \in (0, 1]$ is the fractional occupancy of the solenoids or quadrupoles in the lattice period. Equation (38) shows that quadrupole envelope flutter depends strongly on σ_0 and only weakly on η (the maximum variation in $\mathrm{Max}[r_x]/\overline{r_x}$ in η is $\sim 13\%$), whereas solenoidal focused envelope flutter depends both on σ_0 and η with zero flutter for $\eta = 1$ (continuous focusing limit). Note that when σ_0 increases, matched beam envelope flutter also increases.

From the discussions above it is clear that nonlinear effects acting on a particle moving inside and outside the beam core will become stronger for increasing space-charge strength (relatively small σ/σ_0). Nonlinear effects will be further enhanced in periodic focusing lattices due to the matched beam envelope flutter (generally increasing with σ_0). The CP model will be employed in Sec. 3 to

analyze how these effects can lead to large space-charge induced increases in particle oscillation amplitudes for particles moving just outside the matched beam core. Plausible arguments are presented on how strong, chaotic effects leading to the oscillation amplitude increases can produce transport limits in periodic focusing channels[5].

3 Example Application: Matched Beam Transport Limits

Regions of experimentally observed instability for a initially plane equilibrated ($\varepsilon_x = \varepsilon_y$), envelope matched beam in a FODO quadrupole transport channel are shown in Fig. 3 as a function of the undepressed single particle phase advance σ_0 (focusing strength) and the ratio of depressed to undepressed phase advance σ/σ_0 of the rms equivalent beam core (relative space-charge strength)[23,5]. The range of σ_0 is cut off at $\sigma_0 = 180°$, corresponding to the single-particle and centroid stability limit[8]. The envelope instability band is plotted in gray[9] and rules out a broad region of possible operating points with $\sigma_0 > 90°$. Further regions of experimentally observed[23] higher-order instability are shown in red. Operation in these regions is observed to result in rapid statistical rms emittance growth and particle losses. Measured transition points are indicated on the plot and a curve fit to the experimental transition data gives

$$\sigma_0^2 - \sigma^2 = \frac{1}{2}(120°)^2. \tag{39}$$

For FODO quadrupole transport there is little change in these results with variation of quadrupole occupancy η or the absolute scale of the beam (set by the lattice parameters L_p and η, and the emittances $\varepsilon_x = \varepsilon_y$). These results are believed to apply to a wide range of smooth, plane equilibrated initial distribution functions described by a purely transverse Vlasov-Poisson model. Parametric self-consistent simulation studies with a variety of initial distribution functions produce similar conclusions in the lower region of higher-order instability with pronounced emittance growth and particle losses with a limited machine aperture[5]. Points of interest labeled a ($\sigma_0 = 60°$, $\sigma/\sigma_0 = 0.1$; lower σ_0, strong space-charge), b ($\sigma_0 = 95°$, $\sigma/\sigma_0 = 0.67$; high σ_0 and intermediate space-charge), and c ($\sigma_0 = 110°$, $\sigma/\sigma_0 = 0.1$; high σ_0 and strong space-charge) are indicated inside and outside the lower region of higher-order instability.

Poincaré plots in scaled x/r_x and $(x'r_x - r'_x x)/\varepsilon_x$ phase-space coordinates are shown in Fig. 4 for the three points labeled a, b, and c in Fig. 3. The beam cores are envelope matched, and the Poincaré strobes are taken at every lattice period in the middle of focusing-in-x quadrupoles. Particles are launched between quadrupoles (middle of a drift before a focusing-in-x quadrupole) along the x-axis ($y = 0 = y'$) with $x' = r'_x(x/r_x)$. Initial x-coordinates are chosen in

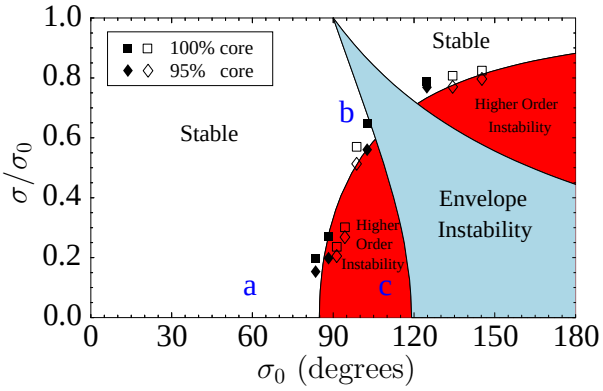

Fig. 3. (color online) Characteristic stability regions in FODO quadrupole transport.

uniform increments from the edge of the beam-core until well outside the core. The Poincaré strobes are initiated after enough lattice periods to allow nonlinearities to shift oscillation phases to decohere the specific choice of initial conditions. Strobes are accumulated over enough lattice periods to throughly sample accessible phase-space. Scaled coordinates employed in the Poincaré plots to reduce the main effects of the matched flutter motion of the beam core in the periodic lattice, rendering the choice of Poincaré strobe phase in the lattice period less critical. The phase-space boundary of the core beam is indicated by the solid green ellipse with unit principal axis radii. Note that the Poincaré phase-spaces appear chaotic in all cases near the core and that higher-order resonant structures appear at large amplitudes well outside the core. At very large amplitudes (beyond the range plotted), the phase-space becomes regular as should be expected when the applied focusing dominates the evolution.

To aid interpretation of the phase-spaces, the same Poincaré plots in Fig. 4 are repeated in Fig. 5 for a limited range of launching amplitudes with $x/r_x \in [1.1, 1.2]$. This change to a limited launch range outside the core helps identify and categorize processes that can result in particles just outside the beam edge evolving to large amplitudes. Particles may evolve just outside the edge of the core due to a large number of processes that are not explicitly investigated (see Sec. 1 discussion). The dashed red ellipses indicate extrapolations of the initial range in phase-space that would occur if the particles evolved with a linear-force Courant-Snyder invariant[12] with values set by the initial conditions. The Poincaré plots exhibit distinctly different behavior when contrasting labeled points a and b (stable region) with c (lower unstable region). For points a and b, particles maintain radial confinement near the initial launch ranges without increasing significantly in maximum excursion measured by x/r_x. For point a, the stronger space-charge nonlinearity results in significantly larger excursions in $(r'_x x - r'_x x)/\varepsilon_x$ with modest increases in x/r_x excursions, while for point b excursions increase little in either phase-space coordinate. In contrast, for the unstable case corresponding to point c, particle oscillation amplitudes

a) $\sigma_0 = 60°$, $\sigma/\sigma_0 = 0.1$

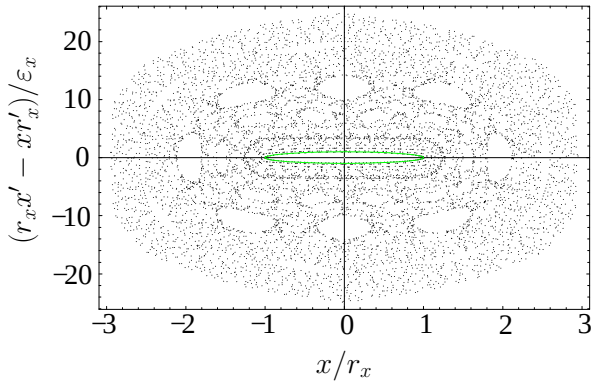

b) $\sigma_0 = 95°$, $\sigma/\sigma_0 = 0.67$

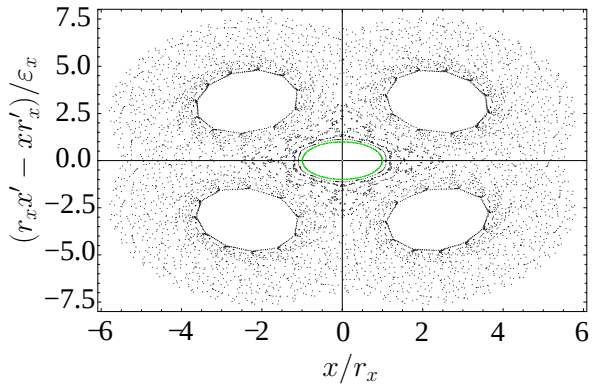

c) $\sigma_0 = 110°$, $\sigma/\sigma_0 = 0.1$

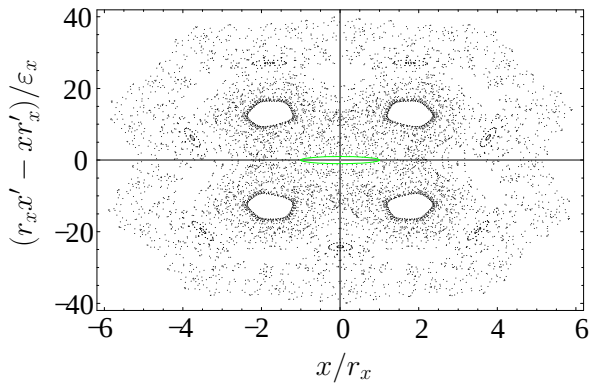

Fig. 4. (color online) Poincaré plots of x/r_x and $(x'r_x - r'_x x)/\varepsilon_x$ phase-space of a FODO matched quadrupole focused beam core for the points a, b, and c labeled in Fig. 3. [$L_p = 0.5$ m, $\eta = 0.5$, and $\varepsilon_x = \varepsilon_y = 50$ mm-mrad]

increase significantly (note the large change in scale) beyond the launch range near the core. Within the lower region of higher-order instability, amplitudes appear to grow until a 4-lobe resonant structure is reached that limits the achieved amplitude growth.

These processes categorized above are halo-like in that they involve particles

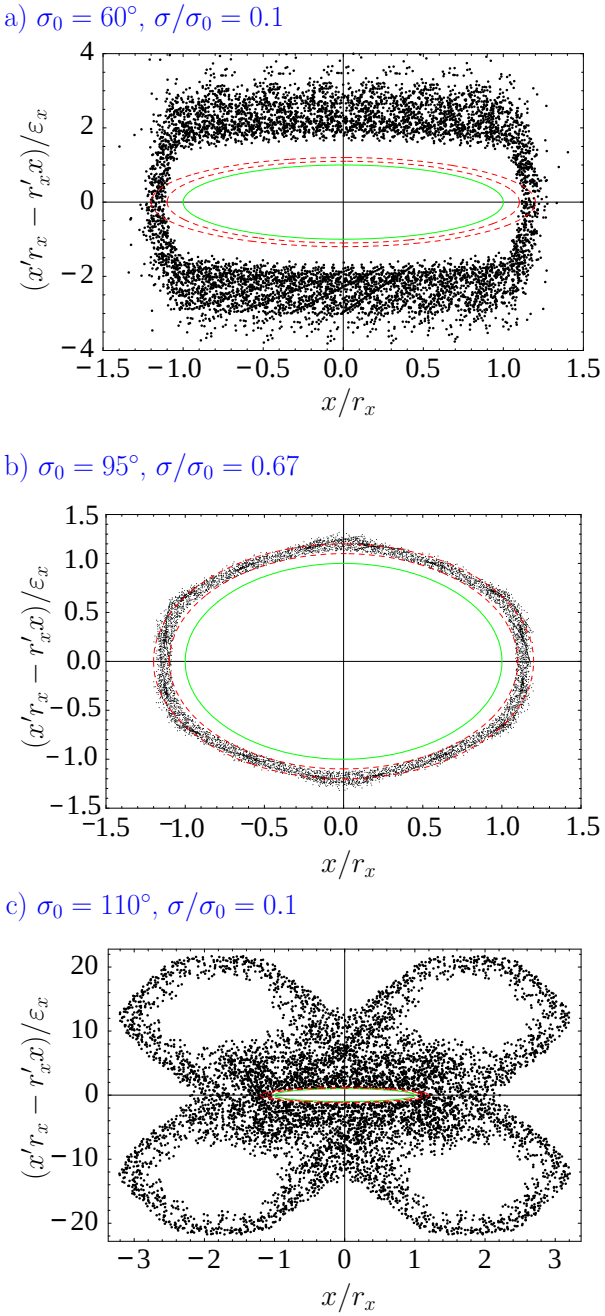

Fig. 5. (color online) Poincaré plots shown in Fig. 4 for particles launched with $x/r_x = [1.1, 1.2]$.

oscillating outside the core. However, they need not only influence tenuous distribution components and may act to significantly perturb the core beam should a significant number of particles participate. If a significant number of particles evolve a small distance outside the rms equivalent beam core in operating regions corresponding to higher-order instability, the large increase in oscillation amplitudes of these particles can produce a blow-up of statistical beam rms emittance and particle losses in machines with a limited aperture.

Because no smooth equilibrium core distribution is known for periodic focusing and injected beams are in any event unlikely to be near any equilibrium form, collective waves within the core resulting from the lack of equilibrium structure provide a ready mechanism to drive enough particles sufficiently outside the core in the high σ_0-regions of observed higher-order instability to degrade transport. The specific number and initial rate of particles increasing in oscillation amplitude will likely depend on the form of the core distribution. But the underlying mechanism of a strongly chaotic region of phase-space induced by strong overlapping resonances which approaches the core in parametric regions of observed higher-order instability will apply to a wide variety of relatively smooth core beams in a fully consistent model. Eventually, these unstable regime processes will also act to degrade the beam core in a fully consistent model. Similar results are observed for particles with space-charge coupled oscillations in both x-x' and y-y' phase space. Detailed expressions of the effect are more complicated in these cases, but the primary characteristics observed for particle oscillations along the principal x- and y-axes persist. Poincaré plots generated by accumulating particles evolving outside the core in fully self-consistent particle-in-cell simulations of a variety of smooth core distributions confirm essential features of the predictions.

To further illustrate characteristics of these results, Figs. 6 and 7 show plots of scaled particle orbits x/r_x and single-particle emittance $\epsilon_x = \sqrt{(x/r_x)^2 + (x'r_x - r_x'x)^2/\varepsilon_x^2}$ evolutions. Cases shown correspond to points a (stable case) and c (unstable case) in Fig. 5. Note that $|x|/r_x = 1$ and $\epsilon_x = 1$ (indicated with green lines on the plots) for a particle at the edge of the beam core. Only a subset of particles employed in the Poincaré plots of Fig. 5 are shown to allow visualization of features. The plots of x/r_x provide a clear measure on how far the particles are evolving outside the core, whereas the single particle emittance plots indicate the corresponding phase-space amplitude of the excursions. In the case of instability, note that a higher density of particle appear to remain nearer to the core (but still with large amplitude) than those that explore the farthest reaches of the limiting resonance [see Fig. 5(c)]. The orbit plots indicate that nonlinear processes quickly decohere the phases of particle oscillations both in the stable and unstable cases. In the unstable case the large particle excursions and large increase in the single particle emittances reinforce the hypothesis that beam quality will be degraded if a significant number of near edge particles participate in these effects. For the case of instability, note that the peak single-particle emittance values are achieved for these initial conditions in a limited number of lattice periods (significant growths in ~ 5 periods and saturation in ~ 15 periods).

The maximum achieved particle oscillation amplitudes in x/r_x for a FODO lattice are contoured in Fig. 8 as a function of σ_0 and σ/σ_0. Maximum amplitudes are calculated from Poincaré plots generated analogously to Fig. 5 for particles launched with two limited ranges of initial values of x/r_x cho-

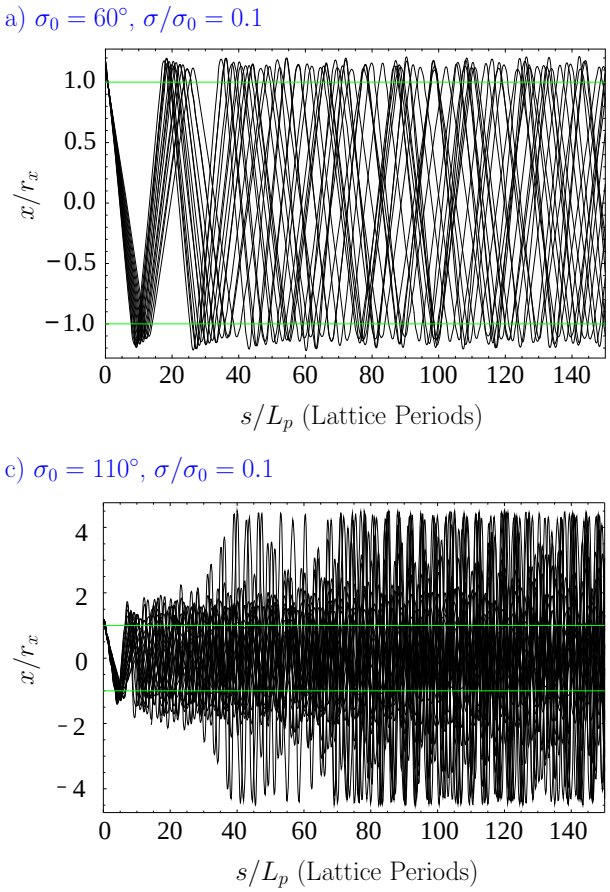

Fig. 6. (color online) Plots of the scaled particle orbits x/r_x versus lattice periods (s/L_p). Particles plotted are a subset of those shown in the corresponding labeled Poincareé plots in Fig. 5.

sen a small distance outside of the matched beam core. The first three black contours are threshold amplitudes [in a) 1.2, 1.3, and 1.4; and in b) 1.3, and 1.4] and the labeled blue contours range from 1.5, 2.0, 2.5, $\cdots$ [max amplitudes are: in a) 11.0 and in b) 11.3]. For reference, the extent of the envelope instability band[9] (band within the solid red curves) and a curve fit to the experimentally measured transition to higher-order instability[23] (dashed red curve) are indicated. Note that the transition to large amplitudes is abrupt when space-charge is strong (small σ/σ_0) and σ_0 increases beyond $\sigma_0 >\sim 85°$. Comparing Figs. 8(a) and 8(b), this transition appears to be relatively insensitive to the specific values of launch radius near the outside of the core. This is in qualitative agreement with observed trends in transport degradation based on simulations and experimental measurements of FODO quadrupole transport lattices (see References contained within Ref. [5]). Operation close to this amplitude transition region will likely result in distribution sensitive degradations in beam quality depending on how many particles evolve significantly outside the core due to a variety of processes (collective waves internal to the core that evolve outside the core, error fields, small mismatches, etc.). For sta-

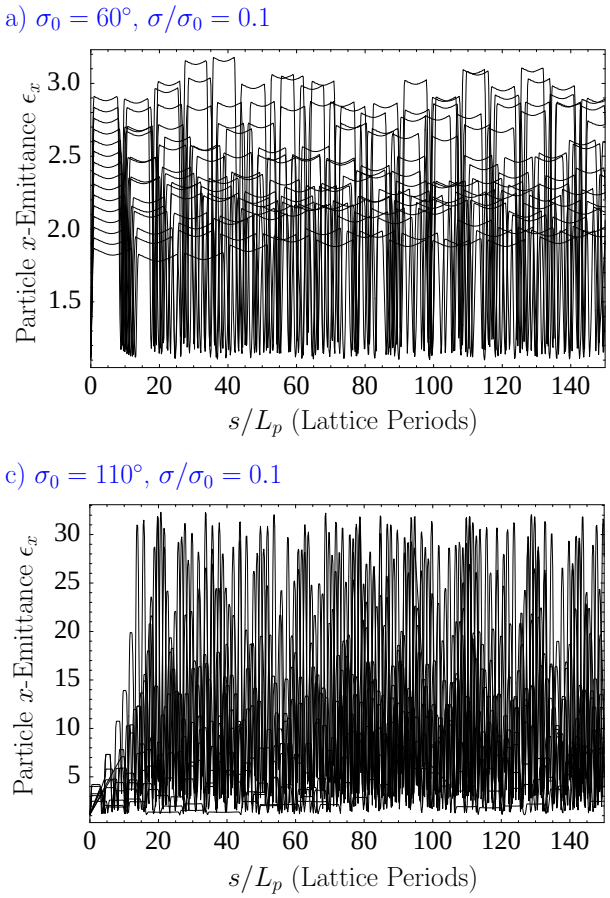

Fig. 7. (color online) Plots of the scaled single particle emittances ϵ_x versus lattice periods (s/L_p). Particles plotted are a subset of those shown in the corresponding labeled Poincaré plots in Fig. 5.

ble transport with respect to higher-order instability for smooth distributions, machine operating parameters can be chosen to avoid regions of large amplitude growth factors. For strong space-charge, this appears consistent with limiting the applied focusing strength to $\sigma_0 < 85°$ which is also consistent with usual design criteria for quadrupole transport of beams with high space-charge intensity. What specific amplitude growth factor can be regarded as sufficiently safe for reliable transport without significant emittance growth or particle losses must likely be investigated on the basis of fully self-consistent simulations. Detailed higher-order stability criteria may require information on the specific form of the core distribution and errors acting on the beam. This becomes especially true if operation is desired close to transition regions with significant amplitude growth factors. In this region one would expect more sensitivity to processes that might drive particles a little outside the beam core.

The CP model employed where the core is a uniform KV beam should be most reliable in a regime of strong space-charge (σ/σ_0 relatively small) where

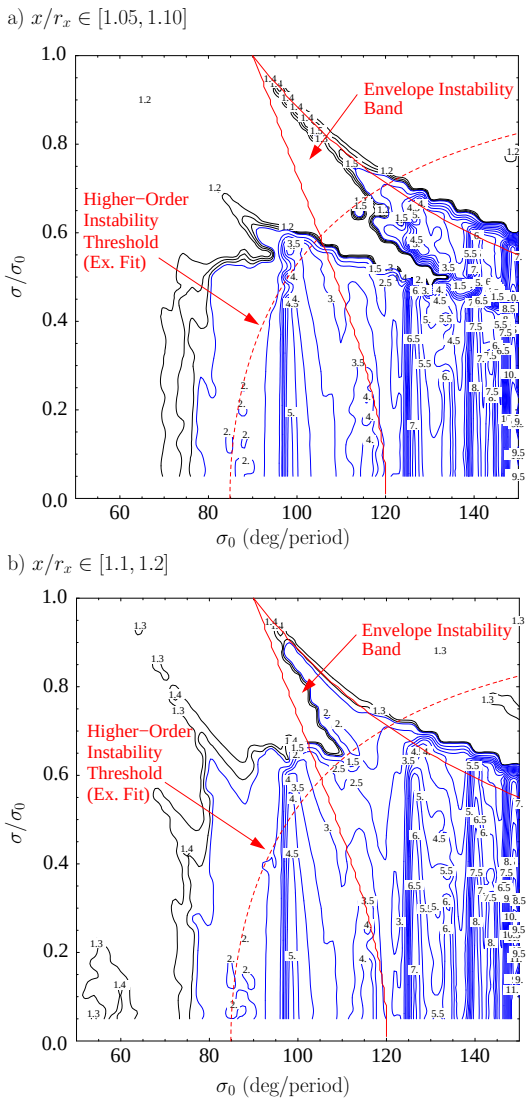

Fig. 8. (color online) Contours of growth in maximum particle oscillation amplitude in x/r_x as a function of σ_0 and σ/σ_0 for particles launched just outside of a matched FODO quadrupole beam. Results are shown for particles launched with a) $x/r_x \in [1.05, 1.10]$ and b) $x/r_x \in [1.1, 1.2]$. [$L_p = 0.5$ m, $\eta = 0.5$, $\varepsilon_x = \varepsilon_y = 50$ mm-mrad]

Debye screening[12] effects are expected to produce a flat beam core out to the sharp edge regardless of the detailed distribution form. Strong, overlapping resonances associated with the transport limits are unlikely to disappear with lesser degrees of model idealization with different core descriptions. Indeed, further fluctuations from internal space-charge waves etc. might be expected for induce enhance chaotic transitions observed in the idealized uniform core model. The use of the CP model should be most reliable in predicting parametric regions with strong higher-order instability induced by the chaotic processes described. However, the CP model is inadequate to address issues of saturation, total emittance growth and particle losses, and core distortions in-

duced by these processes. Comparing Figs. 3 and 8, note that the higher-order instability region above the envelope band found experimentally appears not to be reproduced in the CP model. Likewise, limited data from self-consistent simulations appear not to reproduce this upper, higher-order instability region[5]. It is unclear whether this is discrepancy is due to model limitations in this weak space-charge regime or due to measurement and procedure limitations associated with very high focusing strength (large σ_0) operation of the machine in the experiment. Although this regime is not relevant to the highest space-charge intensity transport, it should be more throughly investigated with self-consistent simulations to verify if higher-order instability induced transport limits are relevant above the envelope band. If so, ring applications where σ_0 is high may be impacted. For example, in fast rotation bunch compressions space-charge may become large enough at peak rotations where the beam could enter an upper region of instability.

Analogous amplitude growth contours to those presented in Fig. 8 for FODO quadrupole transport are shown for matched beam solenoidal transport for lattices of low- and high-occupancy η in Fig. 9. The same contour labeling scheme is employed as in Fig. 8. Particles are launched along the x-axis with $x/r_x = [1.05, 1.10]$ and $x' = r'_x(x/r_x)$. Black threshold contours are labeled 1.2, 1.3, and 1.4 and blue contours are labeled 1.5, 2.0, 2.5, $\cdots$ [max amplitudes are: in a) 4.7 and in b) 1.6]. The extent of the bands of solenoidal focusing envelope instability[9] are indicated on the plots with solid red curves. Note that in contrast to FODO quadrupole focusing (see Fig. 8), there are two distinct bands of envelope instability for solenoidal focusing and the instability bands become broader with decreasing lattice occupancy (η smaller). Although the space-charge and envelope flutter induced growth in particle amplitudes is measured for solenoidal focusing, the effect is much weaker than for quadrupole focusing, particularly for higher lattice occupancies. Moreover, the effect for solenoids, in contrast to quadrupoles, is strongly related to the lattice occupancy. This is not surprising due to solenoidal focusing being weaker which results in less matched beam envelope flutter than quadrupole focusing for a given value of focusing strength (σ_0). In the limit of high occupancy ($\eta \to 1$) solenoidal focusing is equivalent to continuous focusing with a constant matched envelope and no driving mechanism for amplitude increase. For high lattice occupancies and strong space-charge, it appears from Fig. 9(b) that the band of breathing mode instability will act to limit focusing strength before processes leading to near-edge particle amplitude blow-up.

4 Conclusions

An efficient core-particle model has been derived to analyze test particles evolving inside and outside a uniform density elliptical beam. This model

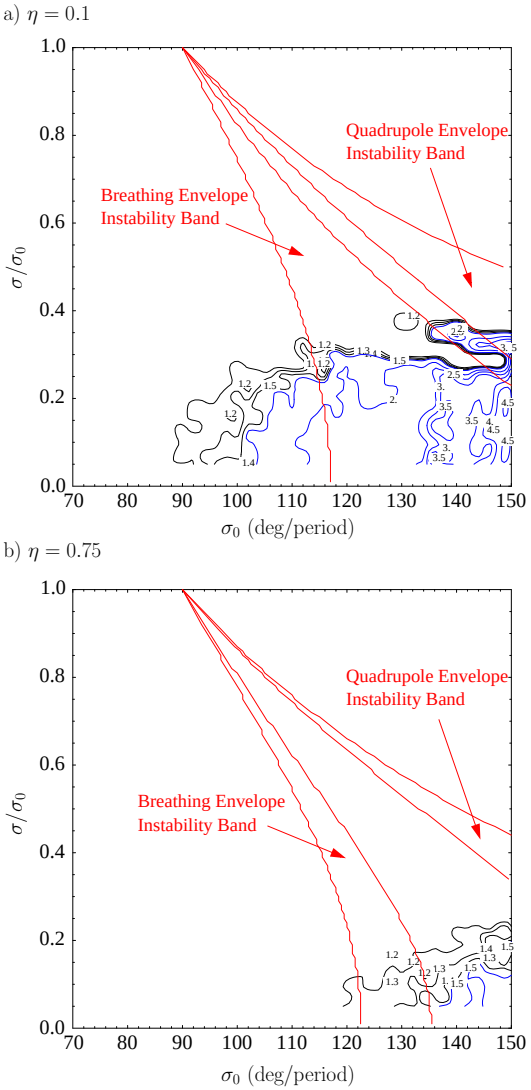

Fig. 9. (color online) Contours of growth in particle oscillation amplitude in x/r_x for particles as a function of σ_0 and σ/σ_0 for a solenoidal focusing lattice with lattice occupancies a) $\eta = 0.1$ and b) $\eta = 0.75$. [$L_p = 0.5$ m, $\varepsilon_x = \varepsilon_y = 50$ mm-mrad]

is expected to be reliable for beams with high space-charge intensity. The edge (envelope) of the core beam can oscillate due to s-varying applied focusing forces (matched envelope flutter) and distribution mismatches of the core. For a given periodic focusing lattice, envelope oscillations tend to become larger as the applied focusing strength of the lattice is increased (i.e., as σ_0 increases). Diagnostics developed show that halo-like particles evolving with amplitudes just outside the beam envelope can experience strong, nonlinear resonance effects when the envelope is oscillating and space-charge intensities are high. These resonances can overlap and orbits near the core can become strongly chaotic, leading to a rapid growth in particle oscillation amplitude. If a significant fraction of particles participate in such effects (non-tenuous halo), statistical rms beam emittance blow-up and significant particle

losses can result, causing degradation of transport that can be interpreted as a higher-order instability. Such transport limits can be reduced by designing lattices and choosing beam parameters where matched envelope oscillations are reduced to the extent possible. Strong (e.g., quadrupole doublet) focusing lattices will generally be more susceptible to such effects than weak focusing (e.g., solenoidal) focusing lattices due to larger intrinsic envelope oscillations with quadrupole focusing. The higher-order instability processes described will be further enhanced by beam envelope mismatch and in cases where there are lattice transitions such as matching sections to decrease beam size since these will act to increase envelope excursions and effective particle phase-advances – which are both driving mechanisms.

Acknowledgments

Boris Bukh and Sugreev Chawla were employed at Lawrence Berkeley National Laboratory as student research assistants during the period when their contributions to this study were made. This work was performed under the auspices of the U.S. Department of Energy by the University of California at Lawrence Livermore and Lawrence Berkeley National Laboratories under Contract Nos. W-7405-Eng-48 and DE-AC03-76SF0098.

References

[1] R. L. Gluckstern, Analytic model of halo formation in high current ion linacs, Phys. Rev. Lett. 73 (1994) 1247.

[2] M. Ikegami, Particle-core analysis of mismatched beams in a periodic focusing channel, Phys. Rev. E 59 (1999) 2330.

[3] T.-S. Wang, Particle-core study of halo dynamics in periodic-focusing channels, Phys. Rev. E 61 (2000) 855.

[4] T. P. Wangler, Beam halo in proton linac beams, in: Proceedings of the XX International Linac Conference, Monterey, CA, 2000, Stanford Linear Accelerator Center, SLAC-R-561, Stanford, CA, 2001, p. 341 and TU202.

[5] S. M. Lund, S. R. Chawla, Space-charge transport limits of ion beams in periodic quadrupole focusing channels, Nuc. Instr. Meth. A 561 (2006) 203.

[6] J.-M. Lagniel, On halo formation from space-charge dominated beams, Nuc. Instr. Meth. A 345 (1994) 46.

[7] J.-M. Lagniel, Chaotic behaviour and halo formation from 2d space-charge dominated beams, Nuc. Instr. Meth. A 345 (1994) 405.

[8] M. Reiser, Theory and Design of Charged Particle Beams, John Wiley & Sons, Inc., New York, 1994.

[9] S. M. Lund, B. Bukh, Stability properties of the transverse envelope equations describing intense ion beam transport, Phys. Rev. Special Topics - Accelerators and Beams 7 (2004) 024801.

[10] Q. Qian, R. C. Davidson, C. Chen, Chaotic particle motion and halo formation induced by charge nonuniformities in an intense ion beam propagating through a periodic quadrupole focusing field, Phys. Plasmas 2 (1995) 2674.

[11] J. Zhou, B. L. Qian, C. Chen, Chaotic particle motion and beam halo formation induced by image-charge effects in a small-aperture alternating-gradient focusing system, Phys. Plasmas 10 (2003) 4203.

[12] R. C. Davidson, Physics of Nonneutral Plasmas, Addison-Wesley, Reading, MA, 1990, re-released, World Scientific, 2001.

[13] S. M. Lund, R. C. Davidson, Warm-fluid description of intense beam equilibrium and electrostatic stability properties, Phys. Plasmas 5 (1998) 3028.

[14] S. M. Lund, D. P. Grote, R. C. Davidson, Simulations of beam emittance growth from the collective relaxation of space-charge nonuniformities, Nuc. Instr. Meth. A 544 (2005) 472.

[15] S. M. Lund, S. R. Chawla, Space-charge transport limits in periodic channels, in: Proceedings of the 2005 Particle Accelerator Conference, Knoxville, TN, IEEE Piscataway, NJ 08855, 2005, p. FPAP034.

[16] S. Chandrasekhar, Ellipsoidal Figures of Equilibrium, Yale University Press, New Haven, 1969.

[17] L. D. Landau, E. M. Lifshitz, The Classical Theory of Fields, fourth edition Edition, Pergamon Press, Oxford, 1975.

[18] I. Kapchinskij, V. Vladimirskij, Limitations of proton beam current in a strong focusing linear accelerator associated with the beam space charge, in: Proceedings of the International Conference on High Energy Accelerators and Instrumentation, CERN Scientific Information Service, Geneva, 1959, p. 274.

[19] E. P. Lee, E. Close, L. Smith, Transportable charge in a periodic alternating gradient system, Nuc. Instr. Meth. ?? (1987) 1126.

[20] S. Wolfram, The Mathematica Book, 5th ed., Wolfram Media, 2003.

[21] S. M. Lund, S. H. Chilton, Space-charge transport limits of ion beams in periodic quadrupole focusing channels, Phys. Rev. Special Topics – Accel. and Beams 9 (2006) 064201.

[22] E. P. Lee, Precision matched solution of the coupled beam envelope equations for a periodic quadrupole lattice with space charge, Phys. Plasmas 9 (2002) 4301.

[23] M. G. Tiefenback, Space-charge limits on the transport of ion beams in a long alternating gradient system, Ph.D. thesis, University of California at Berkeley (1986).